Accepted Manuscript

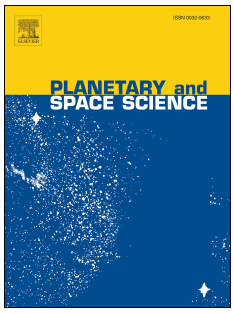

Water vapor deposition from the inner gas coma onto the nucleus of Comet 67P/ Churyumov-Gerasimenko

Y. Liao, R. Marschall, C.C. Su, J.S. Wu, I.L. Lai, O. Pinzon, N. Thomas

PII: S0032-0633(17)30352-5

DOI: 10.1016/j.pss.2018.04.014

Reference: PSS 4519

To appear in: *Planetary and Space Science*

Received Date: 27 October 2017

Revised Date: 14 March 2018

Accepted Date: 14 April 2018

Please cite this article as: Liao, Y., Marschall, R., Su, C.C., Wu, J.S., Lai, I.L., Pinzon, O., Thomas, N., Water vapor deposition from the inner gas coma onto the nucleus of Comet 67P/Churyumov-Gerasimenko, *Planetary and Space Science* (2018), doi: 10.1016/j.pss.2018.04.014.

Water Vapor Deposition from the Inner Gas Coma onto the Nucleus of Comet 67P/Churyumov-Gerasimenko

Y. Liao[1,5], R. Marschall[2,5], C. C. Su[3], J. S. Wu[3], I. L. Lai[4], O. Pinzon[5], N. Thomas[5]

[1]*Space Science Institute, Macau University of Science and Technology, Macau*

[2]*International Space Science Institute, Switzerland*

[3]*Department of Mechanical Engineering, National Chiao Tung University, Taiwan*

[4] *Graduate Institute of Space Science, National Central University*

[5]*Physics Institute, University of Bern, Switzerland*

yliao@must.edu.mo

Abstract

Rosetta has detected water ice existing on the surface of Comet 67P/Churyumov-Gerasimenko in various types of features. One of particular interest is the frost-like layer observed at the edge of receding shadows during the whole mission, interpreted as the recondensation of a thin layer of water ice. Two possible mechanisms, (1) subsurface ice sublimation and (2) gas coma deposition, have been proposed for producing this recondensation process and diurnal cycles of water ice. Previous studies have demonstrated both mechanisms based on simplified models. More precise and modern models are yet insufficient when addressing the gas-coma-deposition mechanism. We aim to study the recondensation from the inner water gas coma of the 67P/Churyumov-Gerasimenko with more physical constraints including the OSIRIS images, nucleus shape model, and insolation conditions. We compute, for the first time, the backflux distributions from the coma with various boundary conditions. Numerical simulations of this gas-coma-deposition process show that the equivalent water ice deposition can be up to several microns in an hour of accumulation time close to the perihelion passage, which is comparable with the simulation results of the other subsurface-ice sublimation mechanism.

Keywords

comets: individual (67P/Churyumov-Gerasimenko) - methods: numerical

1 Introduction

Comets are rich in volatile ices and their sublimation leads to what we observe as cometary activity. Water seems to dominate in coma yet all observed comet nuclei have dark appearance, and only a limited amount of water ice has been detected on some cometary surfaces [Sunshine et al., 2006; Groussin et al., 2013; Oklay et al., 2016]. With in-situ and long-term observations made by Rosetta, water ice has been identified in small patches or bright spots on the surface of Comet 67P/Churyumov-Gerasimenko [Filacchione et al., 2016; Pommerol et al., 2015; De Sanctis et al., 2015]. Furthermore, thin frosts sublimating close to receding shadows have also been observed [De Sanctis et al., 2015; Fornasier et al., 2016]. De Sanctis et al. [2015] have proposed diurnal cycles of water ice with two possible mechanisms to produce observed ice on the surface: (1) ice sublimation from the subsurface layer condensing in the uppermost layer after sunset, or (2) the backflux from the inner coma depositing on the cold area. Prialnik et al. [2008] first used 1D numerical modeling to explore the subsurface ice sublimation process which may explain the outbursts from Comet 9P/Tempel 1. Their results show that, given an active area covered by a thin, porous and poorly conducting dust layer, the ice accumulates on the unilluminated surface (nightside). As time goes by, the accumulation increases, peaks and immediately vanishes soon after sunrise. This mechanism has been widely accepted and adopted by many recent works about Comet 67P/Churyumov-Gerasimenko [e.g., De Sanctis et al., 2015; Fornasier et al., 2016; Filacchione et al., 2016]. The modeling of coma recondensation, on the other hand, has not been extensively explored. Most studies consider coma recondensation mainly for thermo-physical models of the nucleus because the recondensing gas molecules may heat the surface by releasing the latent energy [Crifo, 1987; Tancredi et al., 1994; Davidsson and Skorov, 2004]. Crifo et al. [2003] found coma recondensation possible on the sunlit flanks of a cavity when they investigated the structure of the near-nucleus coma. Rubin et al. [2014] examined the mass transport around the nucleus by modeling the recondensation on the shadowy parts of the nucleus surface. Their simplified models show that the transported mass can be up to a few percent of the total produced mass, and this mass can condense and accumulate on the unilluminated areas. Although the gas coma deposition mechanism has been studied, more precise and modern models for simulation and comparison with observational

results are still not available. Our aim therefore is twofold. First, we compute the backflux distributions from the water gas coma onto the nucleus surface for a variety of initial boundary conditions. Second, we compute the recondensation applicable to Rosetta measurements. The kinetic approach Direct Simulation Monte Carlo (DSMC) [Bird, 1994] has been adopted for simulating the cometary outgassing in the vicinity of the nucleus. The code used in this study, PDSC^{++} [Su, 2013], is the successor of PDSC (Parallel Direct Simulation Monte Carlo) [Wu et al., 2004] and is capable of multi-dimensional flow-field simulation as well as the backflux calculation. It has been proven flexible and useful for studying gas comae under different circumstances [Finklenburg et al., 2014; Liao et al., 2016; Marschall et al., 2016].

The remainder of the paper is organized as follows. Section 2 describes the models and the boundary conditions with the intrinsic physical assumptions, and then illustrates the simulation results corresponding to different test cases. Section 3 presents observational results from Rosetta (based on previous work) that are introduced as additional physical constraints to the models. Uncertainties associated with the models and applicable interpretations of the observations are discussed in Section 4. Finally, Section 5 summarizes and concludes the results.

2 Initial Computations: Models and Results

We start by looking at the relationship between the input boundary conditions and the resulting backflux distributions. To do this, we design several test cases and employ physical models of Comet 67P/Churyumov-Gerasimenko (abbreviated as 67P hereafter) but with simple or general assumptions. We have built an unstructured grid (which defines as a grid with tetrahedral cells) consisting of the nucleus of 67P and the surrounding coma region. The nucleus shape is based on the SHAP2 model released by ESA with a surface area of 39.25 km^2 [Jorda et al., 2016]. The simulation domain extends out to 10 km from the center of the nucleus. A 1D thermal model which simply balances solar input against grey body radiation and sublimation is applied to each facet of the shape model. Thermal conductivity into the interior is ignored. The activity is assumed single species - H_2O - outgassing. The nucleus surface is set to be 100% absorbing, i.e., molecules

which scatter back to the surface would be removed from calculation. Details and discussion of the input physics can be found in Liao et al. [2016].

Table 2.1 The input parameters in test cases. The outgassing forms (insolation-driven; inhomogenous; "measles"), the water gas production rate Q (kg/s), and the heliocentric distance r_H (AU) are given.

* Inferred from Hansen et al. (2016).

Case	Outgassing form	Q [kg/s]	r_H [AU]*
1	Insolation-driven	1.25	3.4
2	Inhomogeneous	1.50	3.4
3	Insolation-driven	19.4	2.0
4	Inhomogeneous: Measles (50%)	1.27	3.4
5	Inhomogeneous: Measles (20%)	1.25	3.4
6	Inhomogeneous: Measles (2%)	1.26	3.4

Table 2.1 displays the different test cases (indicated as Case 1 to 6) with their input parameters. Fig. 2.1 presents the initial boundary conditions of all cases. We define three outgassing forms: insolation-driven, inhomogeneous and measles. For the insolation-driven outgassing, the thermal model mentioned above has been run to compute the production rate from each facet and it is here assumed that the whole nucleus is potentially active. For the inhomogeneous case, an activity pattern has been constructed. We use as a basis, the insolation-driven case result but numerically restrict outgassing to specific areas on the surface which we define in an ad hoc manner. The area definition has been chosen to test various effects within one model run. The "Measles" cases (illustrated as Fig. 2.1d - f) serve as variations of the inhomogeneity of activity. The idea [Liao et al., 2016] is to limit the active areas to smaller regions but boosting their activity to keep the production rate constant. More information of the Measles model can be found in the appendix. We compute the total production rates for the inhomogeneous (Case 2) and the Measles (Case 4 - 6) in an ad hoc manner to keep them comparable to the one of the pre-perihelion, insolation-driven case (Case 1).

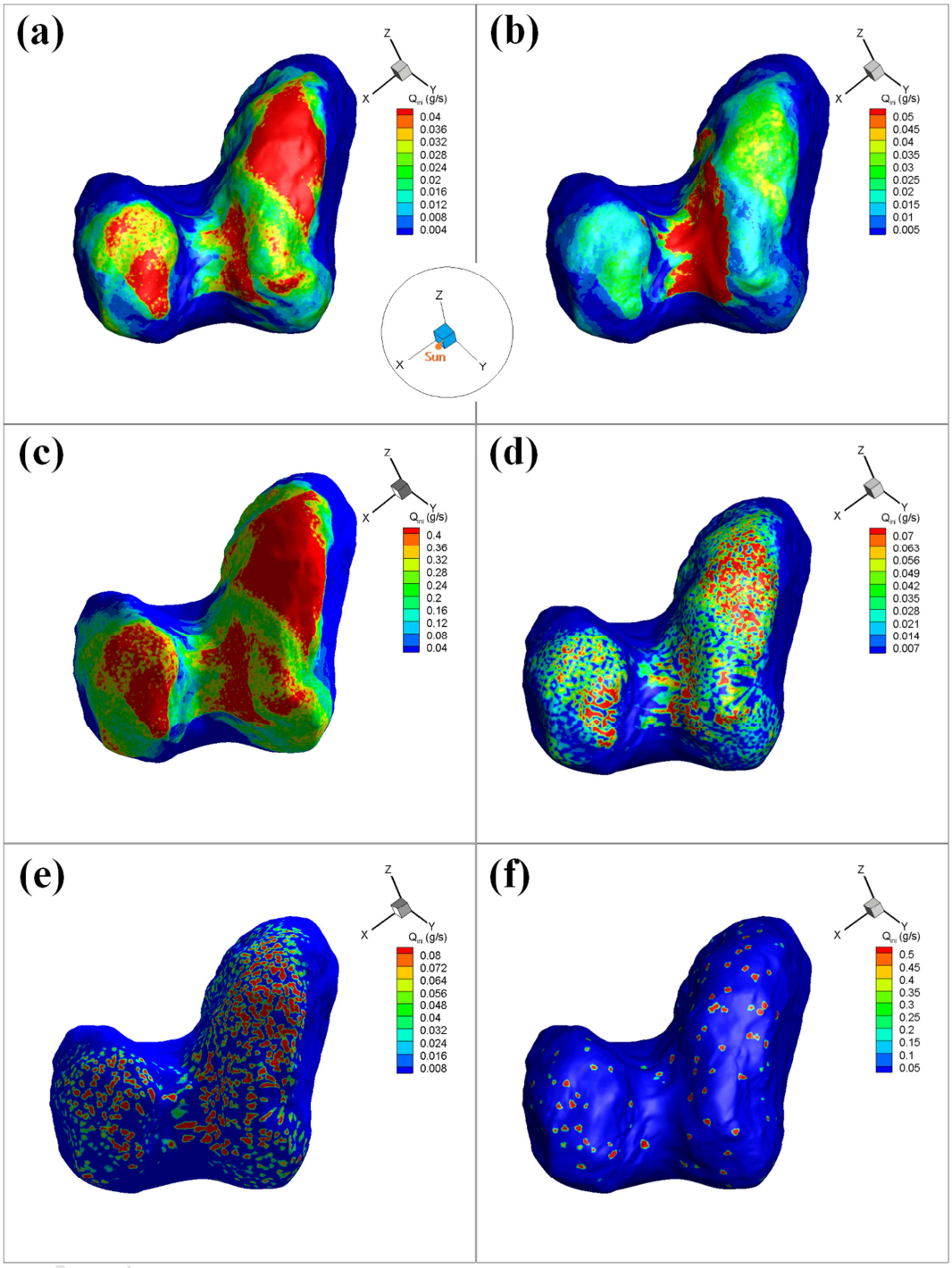

Fig. 2.1 Initial surface production rate distributions of (a) Case 0, (b) Case 1, (c) Case 2, (d) Case 3, (e) Case 4, and (f) Case 5. The direction of the sun is indicated in the schematic view between the plots (a) and (b).

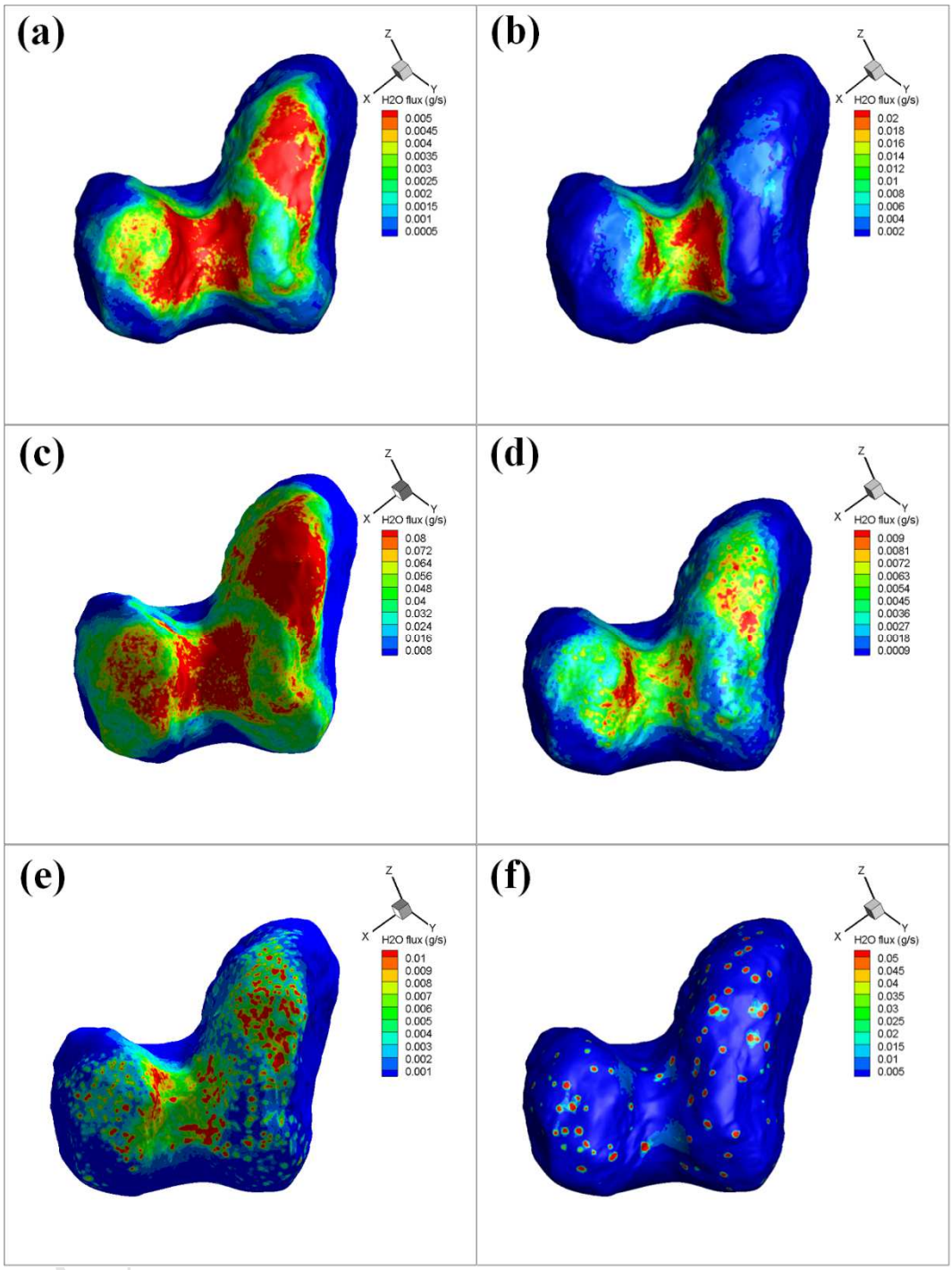

Fig. 2.2 Backflux distributions of (a) Case 0, (b) Case 1, (c) Case 2, (d) Case 3, (e) Case 4, and (f) Case 5.

Fig 2.2 shows the backflux distributions as the simulation results. The backflux is output originally with the unit kg/m^2/s in the code and then transformed into the mass flux with the unit g/s by multiplying by the facet area. For all cases, the backflux is more significant above the dayside than the nightside, as shown in Fig. 2.2. In particular, the backflux is most evident near the active areas and the regions in their vicinity. This is best demonstrated by Case 6 (Fig. 2.2f) with the extreme "measles" outgassing scenario. This is expected since the gas particles are scattered back to the surface through intermolecular collisions, and sufficient numbers of collisions can be ensured by the active areas with high production rates. The backflux also gathers within and around the neck region, which can be seen in Fig. 2.2a – e, as a result of the topography of the comet. The large cavity of the neck may lead the outgassing from active areas impact and condensate on nearby non-active areas [De Sanctis et al., 2015]. The comparisons between the initial production rate distributions (Fig. 2.1a – e) and the backflux distributions (Fig. 2.2a – e) clearly show that some of the produced mass may transport and deposit on the unilluminated areas on the dayside. The recondensation on the nightside, on the other hand, is very limited.

As the cases above perform possible global recondensational scenarios, two additional simulations, Case 1a and Case 1b, are designed to verify local recondensational results. Both cases are set up with a 100% reflecting surface. Note that the "reflecting" here only applies to gas molecules in simulation and does not involve other physical parameters such as surface albedo. Yet 7 facets from different regions (head, body, and neck) on the cometary surface are chosen to be absorptive. The head, the body and the neck are designated based on the x coordinate, and the absorbing facets are randomly selected from the unilluminated facets among the three parts. For Case 1a, the initial boundary conditions of Case 1 (Fig. 2.1a) are used. In Case 1b, the production rate is increased by 2 orders of magnitude higher (125 kg/s) compared to that of Case 1a, which implies a small heliocentric distance close to the perihelion passage (~1.4 AU) in the outgassing simulation. The other boundary conditions of the two cases remain the same. The locations of each absorbing facet are illustrated in Fig. 2.3.

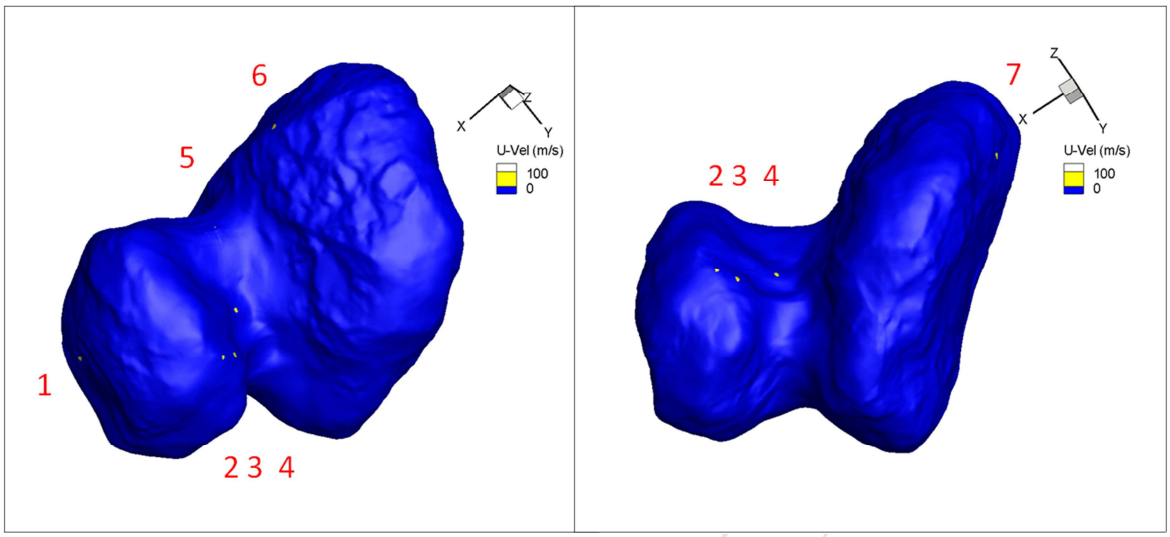

Fig.2.3 The 7 absorbing facets on the surface of 67P as marked in the color yellow. The parameter "U-Vel" only serves as the indication of absorbing facets.

Table 2.2 Information of the absorbing facets. The location (region and Cartesian coordinate), the area A (m^2), the backflux (mg/s) and the ice depth (µm) corresponding to the two cases (Q = 1.25 kg/s for Case 1a and Q = 125 kg/s for Case 1b) are given.

Location	A [m^2]	Backflux [mg/s]		Ice Depth [µm]	
		Case 1a	Case 1b	Case 1a	Case 1b
1/ Head (2278, -592, 151)	201.2	0.050 ±0.019	7.443 ±0.883	0.001 ±3.8E-4	0.143 ±0.017
2/ Head (1231, 17, 1233)	127.3	1.147 ±0.042	105.3 ±2.1	0.035 ±0.001	3.188 ±0.062
3/ Neck (1105, 131, 1069)	237.4	4.997 ±0.151	430.4 ±3.8	0.081 ±0.002	6.987 ±0.061
4/ Neck (764, -54, 550)	162.6	2.613 ±0.198	181.7 ±4.8	0.062 ±0.005	4.306 ±0.113
5/ Neck (363, -749, 167)	14.43	0.014 ±0.005	0.986 ±0.391	0.004 ±0.001	0.263 ±0.104
6/ Body (-744, -1176, 171)	250.4	0.002 ±0.003	0.418 ±0.137	3.7E-5 ±4.2E-5	0.006 ±0.002
7/ Body (-1784, 73, 440)	212.3	0.011 ±0.006	0.777 ±0.052	2.0E-4 ±1.1E-4	0.014 ±0.001

Table 4.5 displays the location, size, backflux and ice depth of all absorbing facets as results. The calculation of the ice depth involves two simple assumptions: (1) the backflux is constant over time, and (2) the backflux condensates as the ice deposition on the surface. We assume, conservatively, the accumulating time of 1 hour. The volume of the ice deposition can then be obtained, and the ice depth can be determined for each facet. All facets present some certain amounts of backflux in both cases. The backflux of Case 1b is in general 2 orders of magnitude larger than the one of Case 1a. Both cases show more water deposition in the neck region. For Case 1b, the ice depths of the facets in the neck region can come to ~7 µm in maximum (e.g., Facet 3) in this 1-hour accumulation time. Given the heliocentric distance 1.4 AU which is close yet to reach the perihelion, the amount of ice would be expected higher than the obtained value in our simulation. However, given the ice deposited on the unilluminated areas on the dayside, the ice may soon sublime and disappear from the surface once these areas are lighted up after the accumulation time.

3 Water Deposition on OSIRIS images: Models and Results

Fornasier et al. [2016] has reported that water frost is found close to the morning shadows in the Imhotep region between June and July 2015, which is very close to the perihelion passage. In addition to Imhotep, potential water frost was also discovered in other regions such as Hapi and Ash with OSIRIS images (Fig. 3.1). One image with visible frost in the Hapi region (Fig. 3.1a) is chosen as a test case for water deposition simulation. It was acquired in December 2014, when 67P is around 2.6 AU from the sun and the H_2O production rate was of the order 5 kg/s [Hansen et al., 2016]. An unstructured grid consisting of the cometary nucleus and the surrounding coma has been constructed to perform DSMC simulations of the gas flow field. SHAP7 [Preusker et al., 2017] was used but decimated to around 150,000 facets for building the nucleus grid. The total surface area of the nucleus is 47.02 km^2 and the average area of a single facet is 332.7 m^2. The simulation domain extends out to 10 km from the center of the nucleus. The orientation of the nucleus was calculated from SPICE kernels, and the resulting boundary conditions were then obtained by the thermal model. The outgassing form is

assumed to be insolation-driven. Like Cases 6 and 7, the test case is designed with a 100% reflecting surface but 5 absorbing facets close or within the Hapi region. According to our calculation, Fig. 3.1a is obtained at the time when the subsolar longitude is about 230°. The absorbing facets are then randomly picked from the areas which is unilluminated but close to the illuminated parts among Hapi. In addition, three more subsolar longitudes - 40°, 130°, and 320° - are chosen to have one full rotation of the comet, i.e., to create "Hapi day/night" scenarios. Table 3.1 lists the total gas production rates and the local times of the four subsolar longitudes. Fig. 3.2 shows the accordingly initial temperature distributions, which clearly illustrate the time variation of the active region on the nucleus surface. All absorbing facets on the nucleus surface are marked in Fig. 3.3.

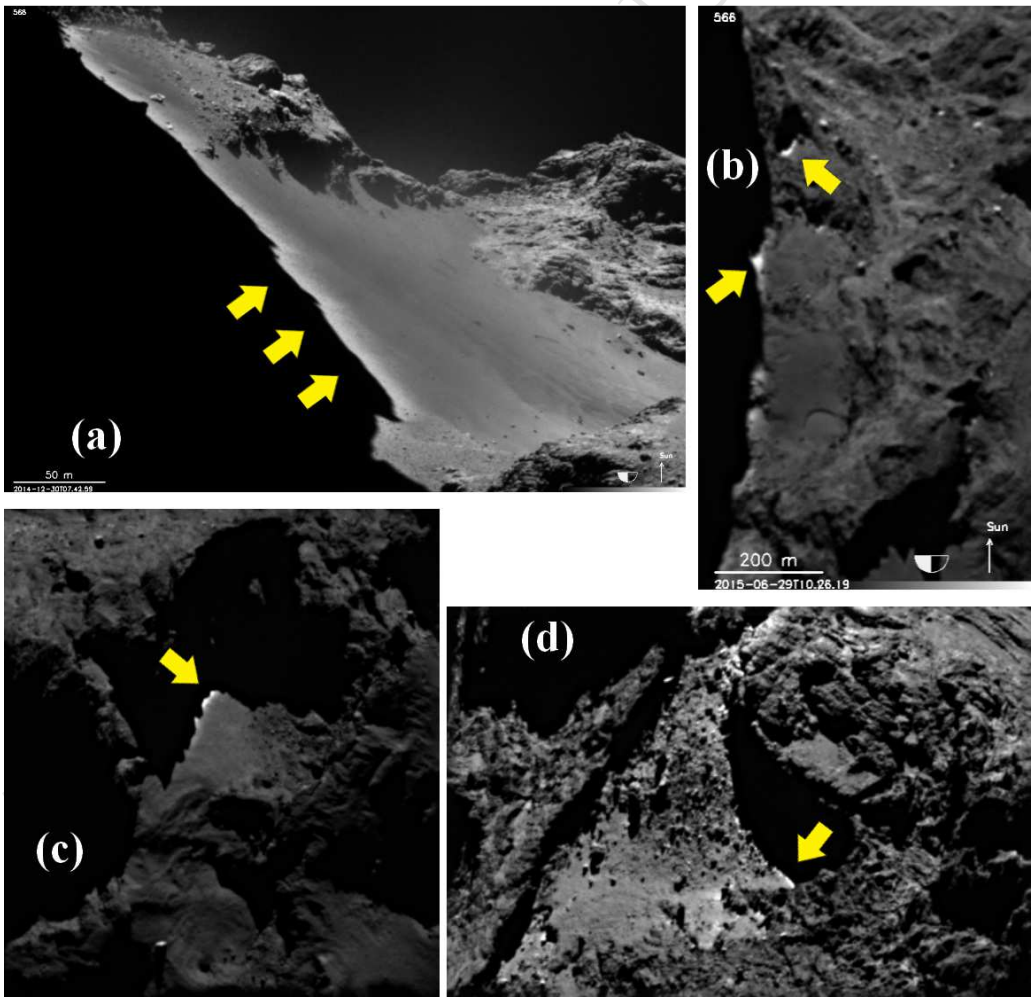

Fig. 3.1 OSIRIS images showing the frost on the fringe of shadow taken in (a) Hapi: 30/12/2014, (b) Hapi: 29/06/2015, (c) Ash: 05/12/2015, and (d) Khonsu-Imhotep border: 12/12/2015. The locations of the frost are indicated by yellow arrows. (Credit: ESA/ROSETTA/OSIRIS)

Table 3.1 The total gas production rate Q (kg/s) versus the subsolar longitude and the local time on Hapi.

Subsolar longitude	Local time of Hapi	Q [kg/s]
40°	Dawn	4.17
130°	Dusk	3.52
230°	Dawn	5.05
320°	Dusk	3.34

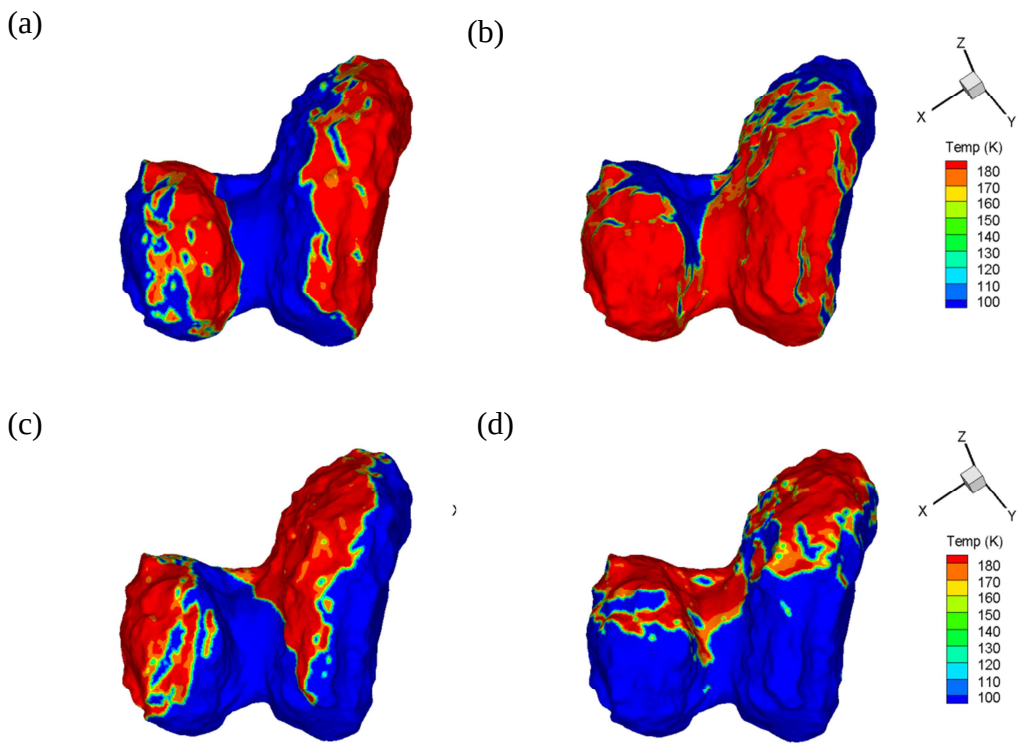

Fig. 3.2 The initial temperature distributions of (a) 40°, (b) 130°, (c) 230°, and (d) 320°.

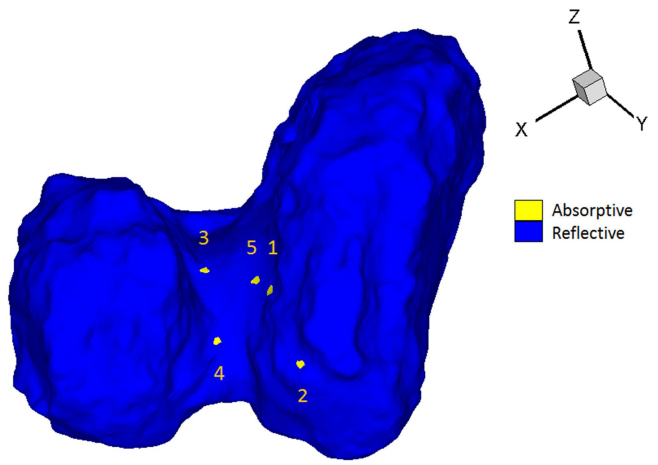

Fig. 3.3 The 5 absorbing facets on the nucleus surface.

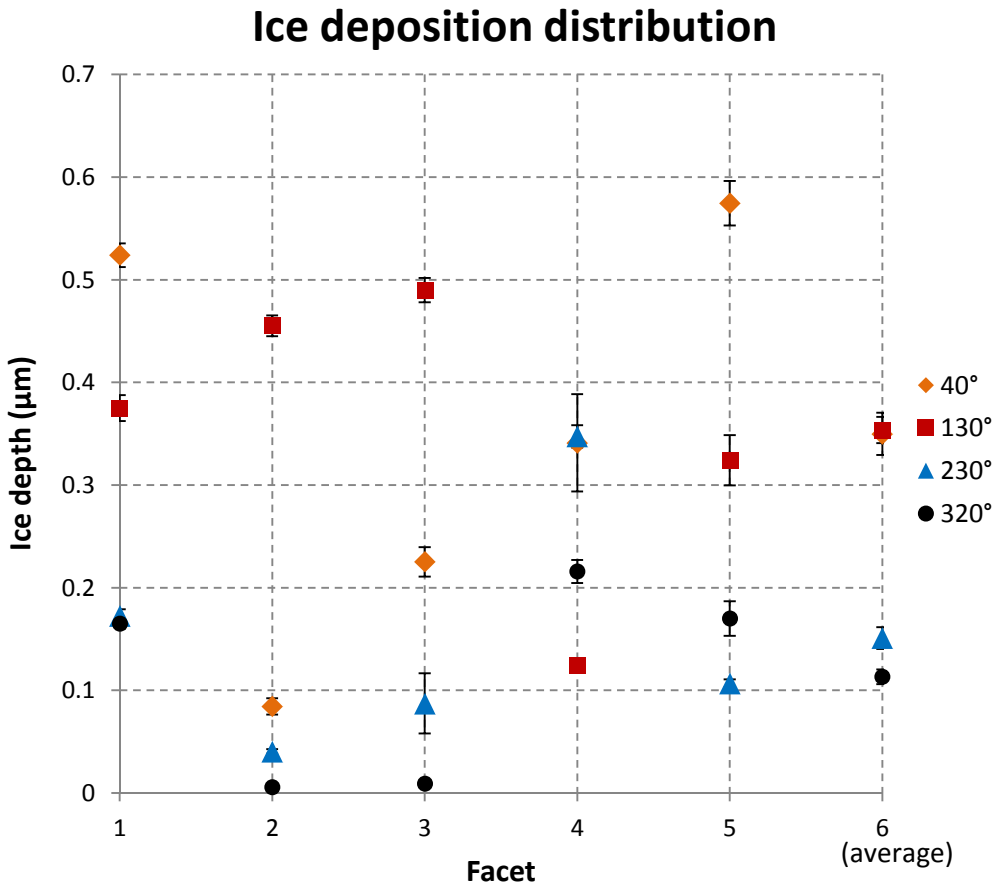

Fig. 3.4 Simulated ice depths (µm) on the 5 facets of the subsolar longitudes 40°, 130°, 230°, 320°. The last column data are the average values of ice deposition on the 5 facets.

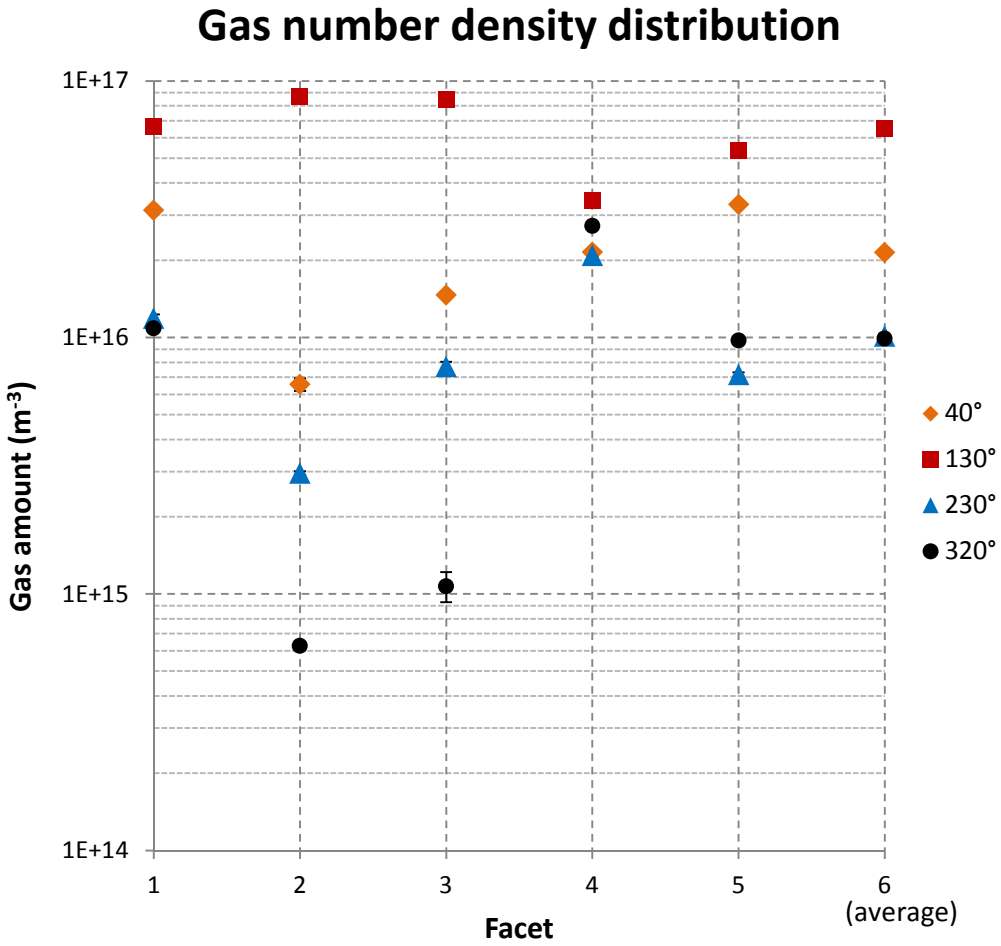

Fig. 3.5 Simulated gas number densities in the 5 cells attached to the surface facets of the four subsolar longitudes. The last column data are the average values of gas amount in the 5 cells.

The simulation results are illustrated as Fig. 3.4 (ice deposition amounts of each absorbing facet) and Fig. 3.5 (gas number densities within the grid cells above the facets). The facet number in the figures can be referred to the numbers specified in Fig. 3.3. Several interesting outcomes can be found here. First, the two plots show that the maximum ice depth and gas number density both happen at the subsolar longitude of 130°, which is the time that most part of Hapi region is active (Fig. 3.2b). Given that the constant backflux and the accumulation time of 1 hour, the ice deposition thickness can reach beyond 0.5 μm for one single facet. The finding of the maximum ice deposition happening on the unilluminated areas at dayside agrees with the results of test cases presented in Section 2. Second, the minimum of the ice depth and gas number density are both obtained at 320°, when Hapi is partially active (Fig. 3.2d). Furthermore, the second highest average amount of ice deposition happens at 40°, when Hapi is almost everywhere inactive (Fig. 3.2a).

This may be explained by the topographic effect of the comet nucleus. For subsolar longitude 40°, one side of the neck region is completely active while the other side is completely inactive. The dark side of cavity may serve as a cold trap which captures the encountering gas particles.

4 Discussion

We successfully simulate the water gas backflux and ice deposition from the inner coma onto the nucleus with various boundary conditions. Indeed, there are many simplifications adopted in the models which could easily result in deviations. We wish to remind that the purpose of the present calculation is to present a viable mechanism for the observed surface water ice deposition, rather than accurately reproduce them. Here the level of generality of these results is commented as follows.

Uncertainties associated with the nucleus shape and gas production model

One major uncertainty in this work would be the shape model used for simulating the water outgassing and backflux in Section 2. As developed in the early stage of the mission, SHAP2 underestimates the surface area by almost 20%, which was a problem for reproducing the observed global production rate. To solve this, an ad hoc manner was adopted to adjust the production rates to the values shown in Hansen et al. (2016). From a large-scale point of view, SHAP2 may be acceptable for modelling global backflux distributions. However, it may not be accurate enough for a small-scale backflux estimation due to the errors in the topographic reconstruction and the illumination conditions on single facets. Other uncertainties lie in the gas production model. Thermal properties such as conductivity and thermal inertia are neglected in the model. Theoretically, the nucleus with the thermal inertia or heat conductivity would result in a lower dayside temperature, a higher nightside temperature, and a higher temperature of the day-night terminator. These changes in local temperatures should modify the local production rates and the resulting backflux amounts. The absorbing/reflecting surface may also play a role in the backflux simulation. For simplicity, most surface facets are defined either absorptive or reflective, which may not be the case for the real comet surface. Last but not least, the assumed 1-hour

accumulation time and the fully transform of gas-to-ice state may be over-simplified in the ice deposition calculation. The points addressed above can all be optimized with more details or physical constraints.

Dependence of the results on the distance between outgassing sources

One may notice that the backflux results of Case 5 (Fig. 2.2e) and Case 6 (Fig. 2.2f) has shown a large discrepancy in the distribution morphology. For Case 5, the backflux covers many of the non-active areas between the active spots, while the limited recondensation fails to fill up the non-active parts for Case 6. An interesting question has therefore arisen: how does the distance between the outgassing sources affect the recondensation? To answer this question, a very simple case with two identical uniformly active sources has been tested. The idea is to design an outgassing environment imitating a local region on 67P but eliminating any possible impact of topography. The sources are two squares 20m on a side, releasing water gas 212.8 g/s as total production rate from the bottom of a cubic box with a side length of 4km. The sizes of the source and background box are decided comparable to the sizes of the surface facets and diameter of 67P. The bottom of the cube is a 100% absorbing plane. The distance between the centers of two squares varies from 2km to 0.5km.

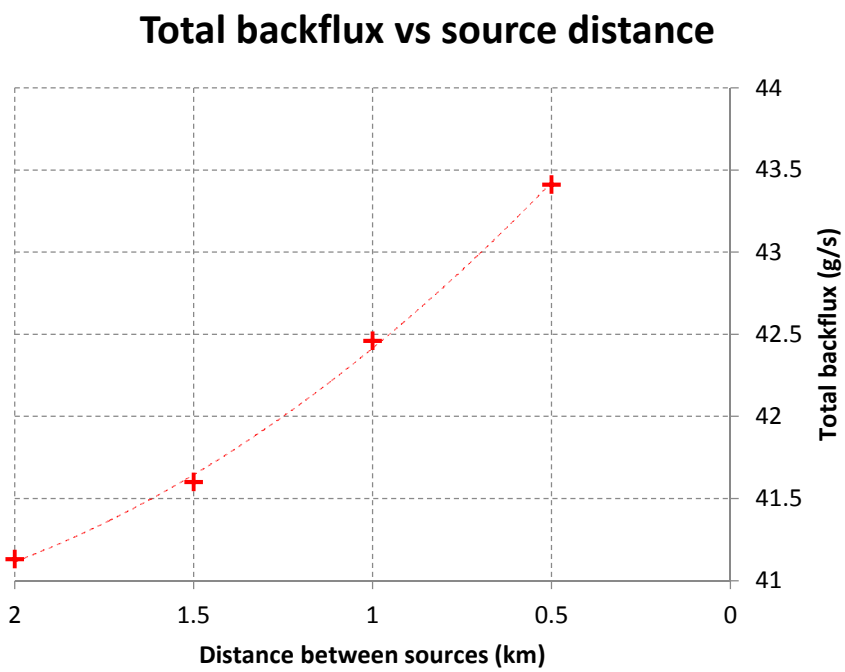

Fig. 4.1 The comparison between the total backflux and the source distance.

Fig. 4.1 shows the total backflux quantity increases with the decreasing source distance. As the two outgassing sources become closer to each other, the recondensation is more likely to cover up the open space (i.e., the non-illuminated area) between them, and the total amount of backflux would get higher. Given that the local production rate of 67P in Case 6 is much lower than our assumption in this case, the distance between the neighbouring outgassing sources would have to decrease much more in order to create a significant backflux distribution. The topography of where the outgassing sources locate would be another important factor affecting the backflux distribution. Intuitively, concave terrains are expected to result in more recondensation compared to flat and convex terrains. The neck part of 67P happens to be a huge cavity, and thus may be able to collect gas particles from both sides.

Interpretation of the results for Rosetta observations

In Section 2, the models approximate the water deposition on a global scale. Our simulation results show that water deposition does exist given a wide range of heliocentric distance (3.4 AU - 1.4 AU). The amount of production rate seems to dominate the amount of deposition. A smaller heliocentric distance gives a higher production rate, which leads to a higher amount of deposition. This can be clearly observed in Fig. 2.2c (Case 3) and the backflux/deposition amounts of Case 1b in Table 2.2. The amount of deposition seems to depend on the distance between outgassing sources as well. It is more likely to create the deposition on the unilluminated areas of dayside or terminator rather than anywhere of nightside. The nightside of the nucleus fails to have deposition because very few gas particles travel to the nightside and chance to have gas-particle-collisions and the resulting backflux is therefore very low. As for Section 3, the results examine the water deposition within a particular region, which is Hapi in this case. Likewise, the amount of production rate seems to determine the amount of deposition. As inferred from Fig. 3.4, the average amount of deposition of Hapi's dawn (40° and 230°) is more than the one of Hapi's dusk (130° and 320°). However, the involving local topography and insolation condition may affect the deposition dramatically, which may explain why the highest average amount of deposition happens at subsolar longitude 130° (Hapi's dusk). One may notice the interesting landform of Hapi as it is adjacent to Hathor cliff and Seth cliff. In principle, water outgassing

from Hapi should collide with these surfaces and create some certain amount of backflux and ice deposition. We do recognize this effect in our simulation results, yet no ice has been observed on Hathor and Seth cliffs. This may be associated with the gravitational potential. Hapi, the gravitational minimum part of the nucleus, can help to attract and accumulate the back falling material such as dust or icy grains [Keller et al., 2017]. The water backflux which meets Hathor and Seth cliffs – places with higher gravitational potentials compared to Hapi – may be unable to stay and accumulate on the cliffs, but fall down to Hapi instead.

5 Conclusion

We summarize hereafter the main lessons of the present results. We have demonstrated that the versatility of PDSC^{++} enables the modelling of recondensation of inner gas coma of 67P. According to our simulation results, it is more likely to have water vapor condensing in non-illuminated regions on the dayside rather than the nightside since the very low production rate of nightside fails to provide large enough numbers of intermolecular collisions to scatter gas particles back to the surface. The neck region of the comet is another preferable place for gas recondensation because of the concave terrain. In addition, the ice deposition acquired from coma recondensation in the near-perihelion environment shows a comparable figure to the ice accumulation from the condensation of subsurface sublimation, which suggests that the coma recondensation mechanism may also play an important role in the hydrological cycle of 67P during its perihelion passage. Finally, the water ice deposition on the surface of 67P resulting from the backflux is modelled, for the first time, based on physical constraints such as OSIRIS images and up-to-date shape models.

Acknowledgements

This work was supported by the Swiss National Science Foundation (SNSF) under grant IZ32Z0_145126 8. We would like to thank Dr. Martin Rubin (University of Bern), Prof. Wing-Huen Ip (National Central University), and Prof. Lou-Chuang Lee (Institute of Earth Science, Academia Sinica) for their insight and expertise that greatly assisted and improved the research.

References

G.A. Bird, Molecular Gas Dynamics and the Direct Simulation of Gas Flows. Oxford University Press (1994)

J.F. Crifo, Improved gas-kinetic treatment of cometary water sublimation and recondensation: application to Comet P/Halley. Astronomy & Astrophysics, 187, 438–450 (1987)

J.F. Crifo, G.A. Loukianov, A.V. Rodionov, and V.V. Zakharov, Navier–Stokes and direct Monte Carlo simulations of the circumnuclear coma II. Homogeneous, aspherical sources. Icarus, 163, 479-503 (2003)

B.J.R. Davidsson and Y.V. Skorov, A practical tool for simulating the presence of gas comae in thermophysical modeling of cometary nuclei. Icarus, 168, 163–185 (2004)

M.C. De Sanctis, F. Capaccioni, M. Ciarniello, G. Filacchione, M. Formisano, S. Mottola et al., The diurnal cycle of water ice on comet 67P/Churyumov-Gerasimenko. Nature, 525, 500–503 (2015)

G. Filacchione, F. Capaccioni, M. Ciarniello, A. Raponi, F. Tosi, M.C. De Sanctis, et al. The global surface composition of 67P/CG nucleus by Rosetta/VIRTIS. (I) Prelanding mission phase. Icarus, 274, 334–349 (2016)

S. Finklenburg, N. Thomas, C.C. Su, and J.S. Wu, The spatial distribution of water in the inner coma of Comet 9P/Tempel 1: Comparison between models and observations. Icarus, 236, 9–23 (2014)

S. Fornasier, S. Mottola, H.U. Keller, M.A. Barucci, B.J.R. Davidsson, C. Feller, et al., Rosetta's comet 67P/Churyumov-Gerasimenko sheds its dusty mantle to reveal its icy nature. Science, aag2671 (2016)

O. Groussin, J.M. Sunshine, L.M. Feaga, L. Jorda, P.C. Thomas, J.Y. Li, M.F. A'Hearn, M.J.S. Belton, S. Besse, B. Carcich, T.L. Farnham, D. Hampton, K. Klaasen, C. Lisse, F. Merlin, and S. Protopapa, The temperature, thermal inertia, roughness and color of the nuclei of Comets 103P/Hartley 2 and 9P/Tempel 1. Icarus, 222, 580–594 (2013)

K.C. Hansen, K. Altwegg, J.J. Berthelier, A. Bieler, N. Biver, D. Bockelée-Morvan, et al., Evolution of water production of 67P/Churyumov-Gerasimenko: An empirical model and a multi-instrument study. Monthly Notices of the Royal Astronomical Society, stw2413 (2016)

L. Jorda, R. Gaskell, C. Capanna, S. Hviid, P. Lamy, J.Ďurech, et al., The global shape, density and rotation of Comet 67P/Churyumov-Gerasimenko from preperihelion Rosetta/OSIRIS observations. Icarus, 277, 257–278 (2016)

H. U. Keller, S. Mottola, S. F. Hviid, J. Agarwal, E. Kührt, Y. Skorov, et al., Seasonal mass transfer on the nucleus of comet 67P/Chuyumov–Gerasimenko. Monthly Notices of the Royal Astronomical Society, 469, S357–S371 (2017)

Y. Liao, C.C. Su, R. Marschall, J.S. Wu, M. Rubin, I.L. Lai, et al., 3D Direct Simulation Monte Carlo modelling of the inner gas coma of comet 67P/Churyumov–Gerasimenko: a parameter study. Earth, Moon, and Planets, 117, 41–64 (2016)

Y. Liao, e. a., in From Giotto to Rosetta – 50th ESLAB Symposium (2016)

R. Marschall, C.C. Su, Y. Liao, N. Thomas, K. Altwegg, H. Sierks et al., Modelling observations of the inner gas and dust coma of comet 67P/Churyumov-Gerasimenko using ROSINA/COPS and OSIRIS data: First results. Astronomy & Astrophysics, 589, A90 (2016)

N. Oklay, J.M. Sunshine, M. Pajola, A. Pommerol, J.-B. Vincent, S. Mottola, et al., Comparative study of water ice exposures on cometary nuclei using multispectral imaging data. Monthly Notices of the Royal Astronomical Society, 462, S394-S414 (2016)

A. Pommerol, N. Thomas, M.R. El-Maarry, M. Pajola, O. Groussin, A.T. Auger, et al., OSIRIS observations of meter-sized exposures of H2O ice at the surface of 67P/Churyumov-Gerasimenko and interpretation using laboratory experiments. Astronomy & Astrophysics, 583, A25 (2015)

F. Preusker e. a., in Asteroids, Comets, Meteors conference (2017)

D. Prialnik, M.F. A'Hearn, and K.J. Meech, A mechanism for short-lived cometary outbursts at sunrise as observed by Deep Impact on 9P/Tempel 1. Monthly Notices of the Royal Astronomical Society: Letters, 388, L20–L23 (2008)

M. Rubin, N. Fougere, K. Altwegg, M.R. Combi, L. Le Roy, V.M. Tenishev, and N. Thomas, Mass Transport around Comets and its Impact on the Seasonal Differences in Water Production Rates. The Astrophysical Journal, 788, 168 (2014)

C.C. Su, Parallel Direct Simulation Monte Carlo (DSMC) Methods for Modeling Rarefied Gas Dynamics. PhD thesis. National Chiao Tung University, Taiwan (2013)

J.M. Sunshine, M.F. A'hearn, O. Groussin, J.Y. Li, M.J.S. Belton, W.A. Delamere, et al., Exposed water ice deposits on the surface of comet 9P/Tempel 1. Science, 311, 1453–1455 (2006)

G. Tancredi, H. Richman, and J.M. Greenberg, Thermochemistry of cometary nuclei. I. The Jupiter family case. Astronomy & Astrophysics, 286, 659–682 (1994)

J.S. Wu, K.C. Tseng, F.Y. Wu, Parallel three-dimensional DSMC method using mesh refinement and variable time-step scheme. Computer Physics Communications, 162, 166–187 (2004)

Appendix: The Measles Model

The purpose of the measles model was to investigate the possible correlation between the inhomogeneity of the active areas and the innermost neutral gas coma of Comet 67P/Churyumov-Gerasimenko. The idea is to "fractionize" the activity which is insolation-driven and uniformly distributed (e.g., Case 1 and Case 3 in Section 1) such that the outgassing comes from discrete facets. Case 1, the case of insolation-driven outgassing, serves as a standard and the surface activity is defined as 100%. Three additional test cases (Case 4, 5, 6) are designed to represent different levels of fractionization, which is defined by the ratio of the total active area to the one of the standard case. The models are nicknamed because of their resemblance to measles. Table A1 lists the production rate, active area, and the corresponding surface activity of Case 1 and all other measles cases.

Table A1 Parameters in different test cases. The gas production rate Q (kg/s), the active area A (km^2), and the defined surface activity (in percentage) are given.

Case	Q [kg/s]	A [km^2]	Surface activity defined as
1	1.25	15.3	100%
4	1.27	7.69	50%
5	1.25	3.06	20%
6	1.26	0.30	2%

Highlights

- A first detailed model of water deposition from the inner coma on the nucleus of Comet 67P/ Chuyumov–Gerasimenko.
- Production rate and topography seem to dominate the amount of deposition.
- Coma recondensation mechanism may play an important role in the hydrological cycle of Comet 67P/ Chuyumov–Gerasimenko during its perihelion passage.